American Mineralogist, Volume 69, pages 902–909, 1984

Surface modification of some titanate minerals subjected to hydrothermal chemical attack

SVERRE MYHRA[1]

Materials Development Division
AERE Harwell, Oxon, United Kingdom

DAVID SAVAGE

Fluid Processes Research Group, British Geological Survey
Nicker Hill, Keyworth, Notts, United Kingdom

ALAN ATKINSON AND JOHN C. RIVIÈRE

Materials Development Division
AERE Harwell, Oxon, United Kingdom

Abstract

Several titanate minerals, $CaTiO_3$, $BaTiO_3$, $BaAl_2Ti_6O_{16}$ and $ZrCaTi_2O_7$, have been subjected to hydrothermal chemical attack (350°C and 500 bars, trace CO_2 in a H_2O-rich medium). The resultant modifications to the solid surfaces and release of atomic species into solution have been studied with surface analytical techniques (SEM, XPS and AES) as well as solution analysis. The data suggest that the alteration of these phases involves: (1) selective leaching of alkaline earth cations by the CO_2-containing fluid, leading to: (2) saturation and subsequent equilibrium precipitation of alkaline earth carbonates. The coexistence of a CO_2-fluid and carbonates effectively buffers P_{CO_2}, pH and the concentration of alkaline earths in the fluid phase.

Introduction

"SYNROC" is the name given to a crystalline titanate mineral assemblage proposed for the encapsulation of high-level radioactive waste (Ringwood, 1978). SYNROC B is the term given to the version consisting of perovskite ($CaTiO_3$), hollandite ($BaAl_2Ti_6O_{16}$), and zirconolite ($ZrCaTi_2O_7$). The basic titanate matrix doped with simulated high-level radioactive waste (HLW) is referred to as SYNROC C. This mineral assemblage was originally chosen not only for its capacity to hold most HLW radionuclides as lattice-bound solid solutions, but also for its apparent resistance to attack by aqueous solutions (Ringwood et al., 1979).

Nesbitt et al. (1981) showed, from theoretical considerations, that Ca-perovskite (and its Sr and Ba analogues) is thermodynamically unstable in many natural groundwaters due (principally) to two decomposition reactions:

$$\underset{\text{perovskite}}{CaTio_3} + SiO_2(aq) = \underset{\text{sphene}}{CaTiSiO_5} \qquad (1)$$

$$\underset{\text{perovskite}}{CaTiO_3} + CO_2(g) = \underset{\text{rutile}}{TiO_2} + \underset{\text{calcite}}{CaCO_3} \qquad (2)$$

As most analyzed groundwaters contain both dissolved silica and carbon dioxide to a greater or lesser degree, it is of fundamental importance to the understanding of SYNROC behavior that the mechanisms of titanate breakdown as a result of attack by a siliceous and/or carbonated fluid phase be understood.

In this study, the dissolution behavior of the individual SYNROC minerals (and of the Ba-analogue of perovskite) in a high temperature CO_2-bearing fluid phase are examined. In particular, surface analytical techniques have been employed to determine changes in composition of the titanate surfaces. This work follows from a similar study on SYNROC B and C specimens (Myhra et al., 1984), and from a more fundamental surface analytical study on the individual titanate minerals (Myhra et al., 1983a,b).

Experimental

The instrumentation, characteristics of specimens and the relevant surface analytical techniques have been described elsewhere (Myhra et al., 1983a,b). Briefly, the titanates were made by cold pressing and sintering raw materials at

---

[1] Permanent address: School of Science, Griffith University, Nathan, Queensland, Australia.

0003–004X/84/0910–0902$02.00

temperatures of 1280°–1400°C for 2–16 hours. Examination by Scanning Electron Microscopy (SEM), X-ray diffraction (XRD) and Energy Dispersive X-ray analysis revealed substantial porosity in all phases and the occurrence of perovskite and alumina as minor phases in zirconolite and hollandite, respectively.

Disc-shaped specimens approximately 10 mm in diameter and 2 mm in thickness were prepared from polycrystalline billets. One surface was always freshly polished using 1 μm diamond paste. The other surfaces were left as cut by a diamond saw. Each specimen was cleaned separately in an ultrasonic methanol bath before being sealed in a gold capsule with de-ionized water in an approximate 2.5:1 rock/water ratio (by mass). As capsules produced by this technique always contain an air void above the level of the fluid phase, atmospheric CO_2 will have been one of the reactants in the experiments. The starting fluid contained less than 4 ppm CO_2 and had a pH of approximately 5–6. The capsules were then loaded into a large volume, "cold-seal", argon pressurised autoclave, and heated to the required temperature. Techniques and procedures were as described by Savage and Chapman (1982). Runs were carried out at 300° and 350°C at a total confining pressure of 500 bars. These temperatures are in excess of proposed values for most conceptual repository designs, but serve to provide the most severe examination of SYNROC behavior under aqueous attack. Runs were terminated with a compressed air quench (not isobaric), after which the capsules were opened and the fluid removed for pH measurement by selective ion electrode, and chemical analysis by ICP (Inductively Coupled Plasma Emission). A number of samples was also analyzed for total carbon using a total inorganic carbon analyzer. The solid specimens were dried in air for a few hours at 70°C and then mounted for surface analysis.

Although the use of quench-type experimental techniques introduce the possibility of the modification of solid and fluid products during the quench process, overall trends of geochemical reactions are generally preserved by this method (Hajash and Archer, 1980). In these experiments, the preservation of alkaline earth carbonates as solid run products (see below) which have inverse solubility relationships with temperature (i.e., their solubility decreases with increasing temperature) cannot be an artifact of the quench process.

For the analyses by XPS (X-ray Photoelectron Spectroscopy), detailed scans were performed over the energy regions encompassing the principal peaks of the constituent atomic species of each mineral. The abundances of surface species could be fully quantified from the peak areas, and alterations to the chemical environment of the species could be inferred from considerations of binding energies and peak shapes. To obtain information about changes in composition as a function of depth, the specimens were ion beam eroded before and after hydrothermal attack and XPS analysis performed for all species after each ion etch. Since the procedures for ion bombardment and XPS analysis were always the same, the differences in composition profiles before and after hydrothermal attack represent real changes caused by the chemical reactions. AES (Auger Electron Spectroscopy) coupled with recording of in-situ SEM (Secondary Electron Microscopy) images provided additional information with a lateral resolution approaching 1 μm in favorable cases.

The details of the hydrothermal runs are listed in Table 1. XPS analyses of specimens from Runs No. 1, 3, 5 and 7 were used to obtain depth profiles of all species as functions of sputtering dose while details of binding energies and peak shapes came from Runs No. 2, 4, 6 and 8. AES spectra and SEM features were recorded for specimens from Runs 3 and 5. Finally, solution analysis and measurement of final pH and total inorganic carbon (expressed as CO_2) were performed for Runs 2, 4, 6, 8 and 9–12.

Table 1. Details of the hydrothermal runs

Mineral	Run	Temp. (°C)	Solution vol. (cc)	Duration (days)	V_1/S_s (cm)*
$CaTiO_3$	1	300	5.0	19	6.5
	2	350	3.5	12	5.0
	9	"	4.0	14	5.0
$BaAl_2Ti_6O_{16}$	3	"	2.0	14	1.7
	4	"	3.5	12	3.0
	10	"	4.0	14	3.3
$ZrCaTi_2O_7$	5	"	2.0	14	1.7
	6	"	3.5	12	3.0
	11	"	4.0	14	3.3
$BaTiO_3$	7	"	5.0	8	6.5
	8	"	3.5	12	5.0
	12	"	4.0	14	5.0

*Confining pressure for all runs was 500 bars. V_1 is the volume of liquid and S_s the geometric surface area of the solid.

Results

Composition profiles by surface analysis

Composition profiles obtained by quantitative XPS analysis of leached and unleached titanates are shown in Figures 1, 2, 3 and 4. These curves represent one of several equivalent sets of analyses. All features shown in the figures are repeatable. The deviations from expected bulk abundances after $\Sigma D \sim 1000$ μA min are the result of systematic errors associated with the choice of sensitivity factors and possible effects of preferential sputtering (ΣD is the integrated dose). These systematic errors are thought to be independent of the effects of hydrothermal attack. Precise determination of sputtering rates for a given atomic species in a particular compound is in general not readily obtained. However, the present apparatus has been used for XPS analysis of a wide variety of chemical compounds; this accumulated experience suggests that 1 μA min dose is roughly equivalent to the removal of 0.2 nm of material. This estimate is unlikely to be in error by more than a factor of two and the

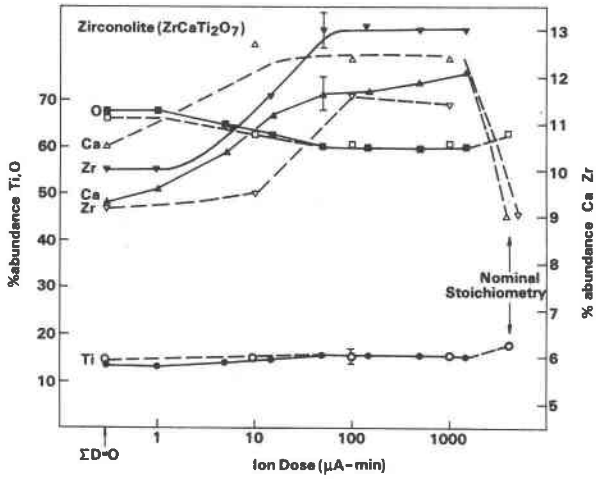

Fig. 1. Composition profiles by XPS of zirconolite before (open symbols and broken lines) and after (filled symbols and continuous lines) hydrothermal attack (run 5 in Table 1). The abundances of the initial surfaces correspond to $\Sigma D = 0$ while the nominal stoichiometries are shown on the right. Conservative and typical statistical error bars are shown for the profiles.

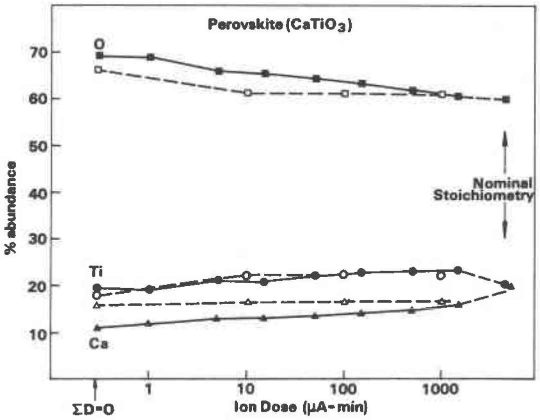

Fig. 3. Composition profiles by XPS of perovskite before (open symbols and broken lines) and after (filled symbols and continuous lines) hydrothermal attack (run 1 in Table 1). The abundances of the initial surfaces correspond to $\Sigma D = 0$ while the nominal stoichiometries are shown on the right. Conservative and typical statistical error bars are as for the zirconolite profiles.

discussion of the results has deliberately been framed so as to be independent of the "actual" sputtering rates. The following observations may be made about the effects of chemical attack on the near-surface composition.

$ZrCaTiO_2O_7$: Ca was depleted to a depth corresponding to Σ D > ~1000 μA min, but Zr may be enriched to still greater depths.

$BaAl_2Ti_6O_{16}$: O was enriched while Ti was correspondingly depleted to a depth corresponding to $\Sigma D = 200$ μA min. Al was enriched to a depth corresponding to $D \approx 10$ μA min; another run on the same material showed similar but more substantial enhancement of the Al abundance near the surface. Ba was depleted to a depth equivalent to as much as $\Sigma D = 1000$ μA min.

$CaTiO_3$: The Ti abundance was essentially unchanged. Ca was depleted to a depth equivalent to $\Sigma D \approx 1000$ μA min while O was similarly enriched.

$BaTiO_3$: Ba and Ti were slightly depleted while O was

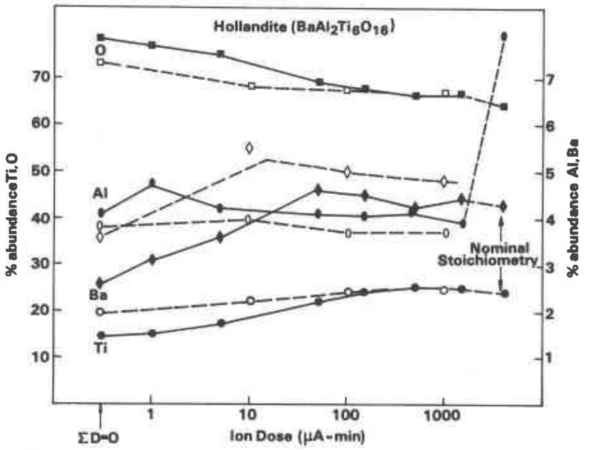

Fig. 2. Composition profiles by XPS of hollandite before (open symbols and broken lines) and after (filled symbols and continuous lines) hydrothermal attack (run 3 in Table 1). The abundances of the initial surfaces correspond to $\Sigma D = 0$ while the nominal stoichiometries are shown on the right. Conservative and typical statistical error bars are as for the zirconolite profiles in Fig. 1.

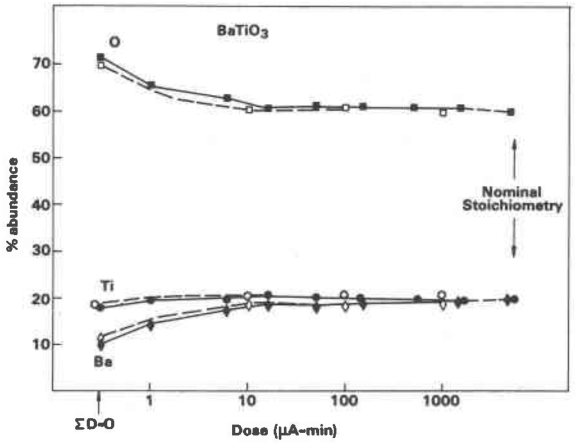

Fig. 4. Composition profiles by XPS of $BaTiO_3$ before (open symbols and broken lines) and after (filled symbols and continuous lines) hydrothermal attack (run 7 in Table 1). The abundances of the initial surfaces correspond to $\Sigma D = 0$ while the nominal stoichiometries are shown on the right. Conservative and typical statistical error bars are as for the zirconolite profiles.

slightly enriched to a depth equivalent to $\Sigma D = 10–20\ \mu A$ min. A second, longer, hydrothermal run (Run 8), led to a more substantial depletion of Ba while O was correspondingly further enriched.

The positions of XPS peaks (i.e., the electron binding energies) and the shapes of their envelopes are sensitive to the chemical state and local environment of the species from which they originate. The binding energies corresponding to major XPS peaks before and after hydrothermal attack are shown as functions of ion dose in Figure 5. The pre-attack results were obtained from a previous surface analytical study of the separate titanate minerals (Myhra et al., 1983a). It can be seen that the reproducibility of peak positions was better than ±0.2 eV and that there were no detectable shifts resulting from hydrothermal attack. No major effects of hydrothermal attack on the envelopes of principal peaks were found, although small but significant effects were observed as described below. In Figures 6 and 7 are shown the peak shapes before and after attack for Ti 2*p* in $CaTiO_3$ and $ZrCaTi_2O_7$, and Ca 2*p* in $CaTiO_3$ and $ZrCaTi_2O_7$. These peak shapes were obtained after a light ion beam etch ($\Sigma D = 10$) which served mainly to remove surface contamination. Effects of bombardment dominated for higher doses. The shapes of the Ba and Zr 3*d* envelopes were not noticeably affected by either irradiation or chemical attack, and are therefore not shown. Also, the Ti 2*p* envelopes in the two perovskites were similar to each other, but different from those for hollandite and zirconolite which showed no detectable changes. The results in Figures 6 and 7 represent a small, but significant, selection from a large body of data on peak shapes for all atomic species in four titanates at various stages of hydrothermal attack and ion beam damage. The effects of ion beam bombardment on the Ti and Ca 2*p* envelopes have been considered in more detail elsewhere (Myhra et al., 1983a). Simple peak stripping by removal of gaussian components is shown in Figures 6 and 7 for two major peaks. In general, it was found that the effect of leaching was to decrease the contribution of high-binding energy components to the Ca 2*p* envelope but to increase it for the Ti 2*p* envelope.

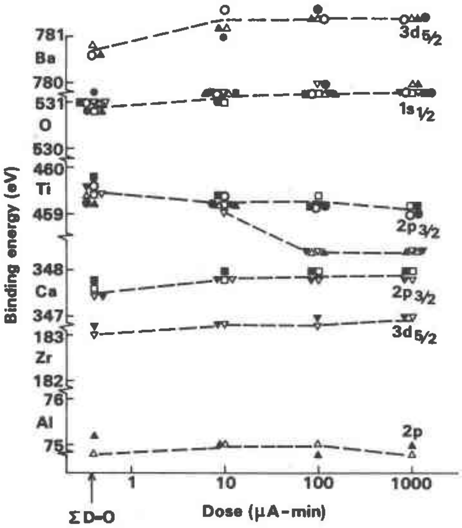

Fig. 5. Binding energies corresponding to positions of major XPS peaks before (open symbols) and after (closed symbols) hydrothermal attack as functions of ion dose. □ = $CaTiO_3$, Q = $BaTiO_3$, △ = $BaAl_2Ti_6O_{16}$ and ▽ = $ZrCaTi_2O_7$.

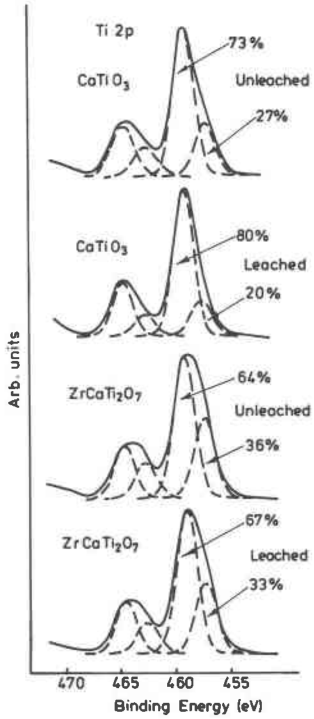

Fig. 6. The effects of chemical attack on the Ti 2*p* envelope for perovskite and zirconolite. Peak stripping procedures resulted in the Gaussian components indicated by the broken curves. The percentages refer to the fractional areas the Gaussian doublets occupy of the total Ti 2*p* envelopes.

High-resolution AES and SEM in combination were used to investigate in detail the features on the surfaces of chemically attacked hollandite and zirconolite (as well as the minority $CaTiO_3$ phase present in the zirconolite samples). Both the SEM images and the AES scans were obtained with the electron source functioning in the high-resolution, low current, mode. The resultant direct pulse-counting spectra could not readily be quantified but were useful for "finger-printing" purposes.

SEM micrographs revealed surface features on the reacted hollandite samples with bright secondary electron contrast. AES analysis of these bright spots showed that their composition was consistent with their being either Al_2O_3 or AlO(OH) with some small amounts of Ti and Ba. The overall surface was found to be somewhat enriched in Al and depleted in Ti and Ba which is in accord with the

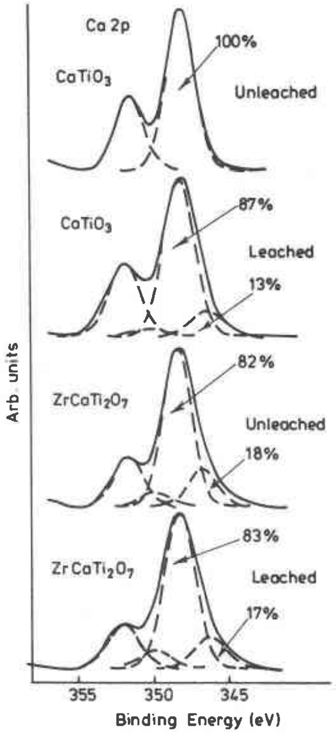

Fig. 7. The effects of chemical attack on the Ca 2*p* envelope for perovskite and zirconolite. Peak stripping procedures resulted in the Gaussian components indicated by broken curves. The percentages refer to the fractional areas the Gaussian doublets occupy of the total Ca 2*p* envelopes.

XPS results. The effects of ion beam bombardment (removal of surface layers) was to bring average abundances, inferred from AES, back to near the nominal hollandite stoichiometry. However, the aluminium-enriched surface features were found to persist to a depth corresponding to at least $\Sigma D = 100\ \mu A$ min.

Similar SEM/AES analysis was carried out for zirconolite (and the attendant perovskite minority phase). This examination revealed a modified patchy layer with bright SEM contrast which was equally likely to overlay both phases. However, the average composition of this layer was similar to that of the bulk material.

Solution chemistry

The results from chemical analysis of the fluid phase are presented in Table 2. It may be seen from Table 2 that contamination of the fluid samples has taken place, e.g., detectable barium concentrations from runs involving perovskite and de-ionized water. This probably occurred through polishing the solid specimens on the same diamond lap. Although each sample was treated ultrasonically with methanol after polishing, it was inevitable that minor, fine grained contaminants would have been present, especially in pores on the unpolished solid sample surfaces.

Table 2. Chemical analyses of the solution phase

	$CaTiO_3$		$BaTiO_3$		$ZrCaTi_2O_7$		$BaAl_2Ti_6O_{16}$	
Run duration (days)	12	14	12	14	12	14	12	14
Final pH (at 25°C)	6.0	5.9	n.d.	7.2	4.5	7.0	6.4	7.6
Ca	1.9	2.5	n.d.	-	n.d.	2.0	1.8	-
Ti	-	-	n.d.	-	n.d.	-	-	-
Al	0.16	0.3	n.d.	0.15	n.d.	0.2	1.2	0.3
Ba	3.2	1.8	n.d.	12.0	n.d.	0.75	8.5	13.0
Zr	-	-	n.d.	-	n.d.	-	-	-
ΣCO_2	97.0	92.0	n.d.	37.0	n.d.	62.0	124.0	202.0

Concentrations are in ppm by weight.
n.d. = not determined.
Detection limits for Ca, Ti, Al, Ba, Zr and CO_2 were 0.006, 0.04, 0.02, 0.0008, 0.002 and 4 ppm, respectively.

Solubility constraints for mechanisms of titanate dissolution

Nesbitt et al. (1981) pointed out that the rate and nature of titanate dissolution will be governed by the degree of solubility of the products of decomposition. For these experiments, the following equilibria are of relevance:

$$\underset{\text{perovskite}}{CaTiO_3} + CO_2 = TiO_2 + \underset{\text{calcite}}{CaCO_3} \qquad (2)$$

$$CaTiO_3 + H_2O = TiO_2 + Ca(OH)_2 \qquad (3)$$

$$\underset{\text{Ba-perovskite}}{BaTiO_3} + CO_2 = TiO_2 + \underset{\text{witherite}}{BaCO_3} \qquad (4)$$

$$BaTiO_3 + H_2O = Ba^{2+} + TiO_2 + 2OH^- \qquad (5)$$

$$\underset{\text{hollandite}}{BaAl_2Ti_6O_{16}} + CO_2 + H_2O = BaCO_3 + 6TiO_2 + \underset{\text{diaspore}}{2AlO(OH)} \qquad (6)$$

$$\underset{\text{zirconolite}}{CaZrTi_2O_7} + CO_2 = CaCO_3 + ZrO_2 + 2TiO_2 \qquad (7)$$

In order to be able to estimate the degree of saturation of the analyzed fluid samples with respect to these alteration products, a geochemical equilibrium software package, EQ3/EQ6 (Wolery, 1979), has been employed. Taking input solution analytical data, EQ3 will calculate activities of individual ions and complexes present using a thermodynamic data base for the temperature range 0–350°C at either 1 atmosphere/steam-saturation or 500 bar pressures. EQ3 will also calculate the degree of saturation of the fluid phase with respect to 130 mineral phases contained within the thermodynamic data base. The saturation indices for witherite, calcite and diaspore for the analyzed fluids are presented in Table 3. The witherite solubility product was derived from the data base of another distribution-of-species computer program, SOLMNEQ (Kharaka and Barnes, 1973). No suitable thermodynamic data for Ti and Zr species could be found; these species are therefore not included in Table 3.

Table 3. Saturation indices (log ion activity product − log *k*) for selected mineral phases as calculated for the solution samples by EQ3

	$CaTiO_3$		$BaTiO_3$		$CaZrTi_2O_7$		$BaAl_2Ti_6O_{16}$	
Run duration (days)	12	14	12	14	12	14	12	14
Calcite	-1.0	-1.0	-	-	-	-2.1	-0.7	-
Diaspore	-2.0	-1.7	-	-3.3	-	-2.9	-1.6	-3.4
Witherite	+0.4	0.0	-	-0.2	-	-1.5	+1.3	+1.4
log fCO_2	+1.5	+1.6	-	-2.1	-	-1.8	+1.2	-1.3

Positive and negative values of saturation indices indicate super- and under-saturation, respectively.

Strictly speaking these indices are zero at equilibrium but in practice it is found that the range ±2 is a reasonable practical criterion for the attainment of equilibrium.

It may be seen from Table 3 that the perovskite solutions are approximately in equilibrium with calcite (within the uncertainty of the thermodynamic data). The hollandite solutions are saturated to super-saturated for witherite but slightly undersaturated for diaspore (the stable form of aluminium hydroxide at 350°C). The barium-perovskite solution is approximately saturated with witherite, and the zirconolite solution may be slightly undersaturated with calcite. Therefore the appearance of diaspore, witherite and calcite as alteration products is to be expected from the measured composition of the fluid and the thermodynamic properties of the minerals.

Perovskite stability relationships in relation to carbon dioxide fugacity and temperature are illustrated in Figure 8 (after Nesbitt et al., 1981). Rutile is the stable TiO_2 polymorph at 350°C (Robie et al., 1978) and is therefore included in Figure 8. The log carbon dioxide fugacity calculated for the perovskite solution samples indicates that the experimental conditions were in the stability field of calcite + rutile as opposed to perovskite + CO_2. The presence of calcite as an alteration product has been confirmed by surface analytical investigations (see below).

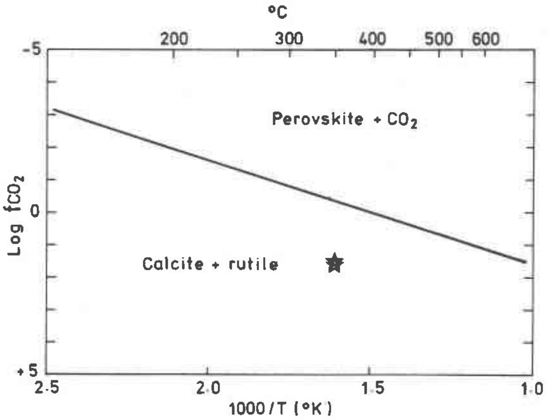

Fig. 8. Perovskite stability relationships in relation to carbon dioxide fugacity and temperature. The symbols show the conditions of the hydrothermal experiments deduced from solution analysis after the experiments (Table 3).

Surface chemical constraints for mechanisms of titanate dissolution

Perovskite

The corroded surfaces showed Ca depletion to a depth of some 200 nm (Fig. 3). Tetravalent Ti was more prevalent in the leached surface than in the original perovskite (Fig. 6) suggesting the presence of TiO_2. This was confirmed by Auger scans of corroded perovskite which showed prominent TiO_2 regions. The presence of carbonate in the modified surface was inferred from XPS data which show that carbon persists to a greater depth in leached specimens. Also it was found that the carbon beyond the first few monolayers in the leached specimen was more tightly bound (as a carbonate) than adventitious graphitic carbon in the surface and near-surface layers. These observations are based on data shown in Figure 9 in which are plotted the percent carbon coverage and the relative binding energy of the center of the C 1*s* peak (BE = BE(O 1*s*) − BE(C 1*s*)) as functions of ion dose. Note that BE for graphitic carbon is about 248 eV while one would expect BE for the carbonate to be about 2 eV less. Also, the Ca 2*p* XPS envelope exhibited a substantial low binding energy component after hydrothermal attack in accord with the notion that $Ca(OH)_2$ was also present on the surface.

Ba-perovskite

The XPS results for this phase showed that the contribution to the Ti 2*p* envelope ascribable to tetravalent Ti

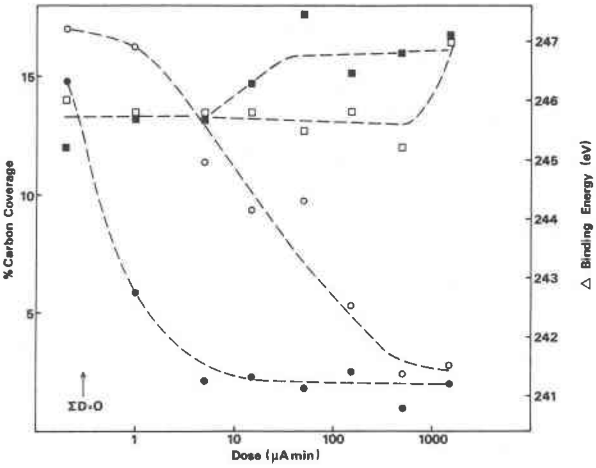

Fig. 9. Carbon coverage and binding energy relative to O 1*s* for leached (open symbols) and unleached (filled symbols) $CaTiO_3$ versus ion dose. The percentage coverage of C is the left ordinate while BE is the right ordinate.

had increased following corrosion. A small, persistent high binding energy component for the C 1*s* peak was also evident, again suggesting the presence of carbonate. Unfortunately, Auger analysis was not applied to this specimen. However, it is likely that the hydrothermal corrosion mechanisms are qualitatively similar for $CaTiO_3$ and $BaTiO_3$.

Zirconolite

The interpretation of the XPS and AES results for zirconolite was complicated by the presence of the minor perovskite phase. Essentially it was found that Zr was enriched, while Ca was depleted by hydrothermal attack, Ti and O remaining unaffected.

Hollandite

XPS results showed that Al was enriched in the surface after corrosion and the AES data were consistent with the enrichment being associated with alumina or aluminium hydroxide (diaspore). The Ti 2*p* XPS envelope showed little change as a result of corrosion and there was no evidence of TiO_2 (rutile) formation on the exposed surface. Likewise, there was no evidence for the presence of $BaCO_3$ on the surface; the abundance, binding energy and peak shape of the C 1*s* peak was consistent with the presence of carbon only as graphitic contamination.

Mechanisms of dissolution

It is apparent from the above descriptions of surface chemistry of corroded specimens and from the evaluation of the saturation state of alteration phases in the analysed leachant fluids, that the mechanisms of dissolution of the titanates examined here are remarkably similar. In general, one can envisage three stages during hydrothermal attack. Using perovskite as a model, these would be: (1) Selective leaching of alkaline earth cations (equation 3), coupled with hydration of the surface layer. This accounts for the initial depletion in alkaline earths in corroded specimens and the observed oxygen enrichment after leaching. (2) Saturation of alkaline-earth carbonates in the fluid phase. As alkaline-earth cations build up in the fluid phase, saturation of alkaline-earth carbonate minerals will eventually be reached if f_{CO_2} is high enough. When the solubility product of these phases is exceeded, precipitation will occur, either on the titanate surface or elsewhere. This accounts for the observed presence of carbonates on the titanate surfaces. (3) Achievement of equilibrium with CO_2 (equation 2). The precipitation of alkaline earth carbonates will reduce the partial pressure of CO_2 in the fluid phase until equilibrium is reached, thus:

$$CaCO_3 + 2H^+ = Ca^{2+} + CO_2 + H_2O \qquad (8)$$

This reaction effectively buffers the CO_2 partial pressure, the alkaline earth cation concentration, and the hydrogen ion activity of the fluid phase.

This sequence of reactions may explain the commonly observed kinetic features of hydrothermal corrosion of SYNROC and titanate minerals; namely the relatively high initial dissolution rates, followed by a progressive decrease in leach rate thereafter to a "plateau" level (Ringwood et al., 1979; Oversby and Ringwood, 1982).

Conclusions

The results of this study indicate, as suggested by Nesbitt et al. (1981), that perovskite, as well as other constituent mineral phases of SYNROC, are initially unstable in the presence of a CO_2-bearing fluid phase under hydrothermal conditions.

However, the SYNROC titanate minerals rapidly equilibrate with this fluid phase through precipitation of alkaline-earth carbonates and the formation of a modified surface layer enriched in TiO_2, ZrO_2 and AlO(OH). The degree of dissolution of the titanates is essentially governed by the solubility of these alteration products in the fluid phase at the prevailing conditions of temperature and pressure.

Acknowledgments

The authors would like to thank Jane Robbins and Tony Milodowski for assistance in preparation of the hydrothermal experiments and the scanning electron microscopy, respectively. Chemical analyses of the fluid samples were performed by W. Temple and D. A. Brown who are thanked for their help. The original manuscript was considerably improved by constructive reviews from J. Clemens, R. L. Hevy and J. White, which the authors gratefully acknowledge. This paper is published by permission of the Director, British Geological Survey (N.E.R.C.). One of the authors (SM) would like to thank the Harwell Establishment and, in particular, the Surface Analysis Section for assistance and hospitality extended during the period of attachment.

References

Hajash, A. and Archer, P. (1980) Experimental seawater/basalt interactions: effects of cooling. Contributions to Mineralogy and Petrology, 75, 1–13.

Kharaka, Y. K. and Barnes, I. (1973) SOLMNEQ: solution-mineral equilibrium computations. U.S. National Technical Information Service, PB214–899.

Myhra, S., Bishop, H. E. and Rivière, J. C. (1983a) Investigation by XPS of surface features of some titanate minerals. Surface Technology, 19, 161–172.

Myhra, S., Bishop, H. E. and Rivière, J. C. (1983b) Surface analytical features of SYNROC B and C. Surface Technology, 19, 145–160.

Myhra, S., Atkinson, A., Rivière, J. C. and Savage, D. (1984 in press) A surface analytical study of SYNROC subjected to hydrothermal chemical attack. Journal of the American Ceramic Society.

Nesbitt, H. W., Bancroft, G. M., Fyfe, W. S. Karkhanis, S. N., Nishijima, A. and Shin, S. (1981) Thermodynamic stability and kinetics of perovskite dissolution. Nature, 289, 358–362.

Oversby, V. M. and Ringwood, A. E. (1982) Leaching studies on

SYNROC at 95°C and 200°C. Radioactive Waste Management, 2, 223–237.

Ringwood, A. E. (1978) Safe disposal of high-level nuclear reactor wastes: a new strategy. Australian National University Press, Canberra.

Ringwood, A. E., Kesson, S. E., Ware, N. G., Hibberson, W. O. and Major, A. (1979) Immobilisation of high level nuclear reactor wastes in SYNROC. Nature, 278, 219–223.

Robie, R. A., Hemingway, B. S. and Fisher, J. R. (1978) Thermodynamic properties of minerals and related substances at 298.15K and 1 bar (10^5 Pascals) pressure and at higher temperatures. U.S. Geological Survey Bulletin 1452.

Savage, D. and Chapman, N. A. (1982) Hydrothermal behaviour of simulated waste glass and waste rock interactions under repository conditions. In G. W. Bird and W. S. Fyfe, Eds., Geochemistry of radioactive waste disposal. Chemical Geology, 36, 59–86.

Wolery, T. J. (1979) Calculation of chemical equilibrium between aqueous solution and minerals: the EQ3/6 software package. Lawrence Livermore Laboratory, UCRL-52658.

Manuscript received, May 17, 1983;
accepted for publication, May 8, 1984.